CORA Cork Open Research Archive
Cartlann Taighde Oscailte Chorcaí

Title	Strain induced large enhancement of thermoelectric figure-of-merit (ZT□#□2) in transition metal dichalcogenide monolayers ZrX2 (X□=□S, Se, Te)
Authors	D'Souza, Ransell;Mukherjee, Sugata;Ahmad, Sohail
Publication date	2019-12-03
Original Citation	D'Souza, R., Mukherjee, S. and Ahmad, S. (2019) 'Strain induced large enhancement of thermoelectric figure-of-merit (ZT□#□2) in transition metal dichalcogenide monolayers ZrX2 (X□=□S, Se, Te)', Journal of Applied Physics, 126(21), 214302 (10pp). doi: 10.1063/1.5125191
Type of publication	Article (peer-reviewed)
Link to publisher's version	https://aip.scitation.org/doi/abs/10.1063/1.5125191 - 10.1063/1.5125191
Rights	© 2019, the Authors. Published under license by AIP Publishing. This article may be downloaded for personal use only. Any other use requires prior permission of the author and AIP Publishing. This article appeared as: D'Souza, R., Mukherjee, S. and Ahmad, S. (2019) 'Strain induced large enhancement of thermoelectric figure-of-merit (ZT□#□2) in transition metal dichalcogenide monolayers ZrX2 (X□=□S, Se, Te)', Journal of Applied Physics, 126(21), 214302 (10pp), doi: 10.1063/1.5125191, and may be found at https://doi.org/10.1063/1.5125191
Download date	2026-11-01 02:17:30
Item downloaded from	https://hdl.handle.net/10468/9441

UCC
University College Cork, Ireland
Coláiste na hOllscoile Corcaigh

Journal of Applied Physics

Strain induced large enhancement of thermoelectric figure-of-merit ($ZT \sim 2$) in transition metal dichalcogenide monolayers ZrX_2 (X = S, Se, Te)

Cite as: J. Appl. Phys. **126**, 214302 (2019); https://doi.org/10.1063/1.5125191
Submitted: 21 August 2019 . Accepted: 13 November 2019 . Published Online: 03 December 2019

Ransell D'Souza, Sugata Mukherjee, and Sohail Ahmad

View Online Export Citation CrossMark

ARTICLES YOU MAY BE INTERESTED IN

Enhancement of the electronic thermoelectric properties of bulk strained silicon-germanium alloys using the scattering relaxation times from first-principles calculations
Journal of Applied Physics **126**, 215103 (2019); https://doi.org/10.1063/1.5117345

Mechanical properties of monolayer ternary transitional metal dichalogenides $MoS_{2x}Te_{2(1-x)}$: A molecular dynamics study
Journal of Applied Physics **126**, 215105 (2019); https://doi.org/10.1063/1.5122264

Carbon pair defects in aluminum nitride
Journal of Applied Physics **126**, 215102 (2019); https://doi.org/10.1063/1.5123049

Lock-in Amplifiers up to 600 MHz
Zurich Instruments
Watch



© 2019 Author(s).

Journal of Applied Physics ARTICLE scitation.org/journal/jap

Strain induced large enhancement of thermoelectric figure-of-merit ($ZT \sim 2$) in transition metal dichalcogenide monolayers ZrX_2 (X = S, Se, Te)

Cite as: J. Appl. Phys. **126**, 214302 (2019); doi: 10.1063/1.5125191
Submitted: 21 August 2019 · Accepted: 13 November 2019 ·
Published Online: 3 December 2019

View Online Export Citation CrossMark

Ransell D'Souza,[1,a)] Sugata Mukherjee,[1,b)] and Sohail Ahmad[2,c)]

AFFILIATIONS

[1]Department of Condensed Matter Physics and Materials Science, S.N. Bose National Centre for Basic Sciences, Block JD, Sector III, Salt Lake, Kolkata 700098, India
[2]Department of Physics, Faculty of Science, King Khalid University, Abha, Saudi Arabia

[a)]**Electronic mail:** ransell.d@gmail.com. **Present address:** Tyndall National Institute, University College Cork, Cork, Ireland.
[b)]**Author to whom correspondence should be addressed:** sugata@bose.res.in and sugatamukh@gmail.com
[c)]**Electronic mail:** sohailphysics@yahoo.co.in

ABSTRACT

Two-dimensional group IV transition-metal dichalcogenides have encouraging thermoelectric applications since their electronic and lattice properties can be manipulated with strain. In this paper, we report the thermoelectric parameters such as electrical conductivities, Seebeck coefficients, electrical relaxation times, and the mode dependent contributions to the lattice thermal conductivity of ZrX_2 (X = S, Se, Te) from first-principles methods. Our calculations indicate that due to tensile strain, the power factor increases while simultaneously decreasing the lattice thermal conductivity, thus enhancing the thermoelectric figure of merit. Tensile strain widens the bandgap, which corresponds to a higher power factor. The lattice thermal conductivity decreases due to the stiffening of the out-of-plane phonon modes, thus reducing the anharmonic scattering lifetimes and increasing the thermoelectric figure-of-merit.

Published under license by AIP Publishing. https://doi.org/10.1063/1.5125191

I. INTRODUCTION

Thermoelectric (TE) conversion can be a very simple and feasible solution to the ever-growing energy crisis, since the waste energy from the by-products of solid-state devices can be directly converted into electricity. TE materials therefore have encouraging applications in power generations and solid-state cooling. Due to different scattering mechanisms in phonons at lower dimensions, low-dimensional materials have been preferred over their corresponding bulk counterparts for an enhanced TE performance.[1–3] For example, monolayers of MX_2 (M = Mo, W; X = S, Se) demonstrate better thermoelectric performances than their corresponding bulks.[4–7] With the advancement in nanotechnology, two-dimensional (2D) materials have been produced successfully.[8,9] Two-dimensional ZrS_2 and $ZrSe_2$ have been experimentally synthesized by Zeng *et al.*[10] and Sargar *et al.*,[11] respectively. Very recently, Tsipas *et al.*[12] have grown 2D $ZrTe_2$ using molecular beam epitaxy on InAs(111)/Si(111) substrates. Development in the synthesis of these low-dimensional materials and the fact that their low-dimensional properties have improved thermoelectric properties have opened up new opportunities in group IV transition-metal dichalcogenides (TMDs) in the field of thermoelectrics.

The conversion efficiency of any thermoelectric material is characterized by its figure-of-merit, $ZT = \frac{S^2\sigma}{\kappa}T$, a dimensionless parameter that depends on the voltage induced by the temperature gradient known as the Seebeck coefficient (S), electrical conductivity (σ), absolute temperature (T), and total thermal conductivity (κ), having contributions from both electrons and lattice vibrations (phonons). Enhancement of ZT is a challenging endeavor since σ, S, and κ are unfavorably related to each other, i.e., larger σ would generally lead to lower S and larger κ, thus lowering ZT.

In recent years, numerous techniques to improve ZT for two-dimensional materials have been examined. These techniques involve defect engineering, n and p-type doping, and inducing strain. For example, Anno *et al.*[13] have enhanced the figure of merit of graphene through defect engineering. Similarly, Tabarraei[14] calculated the

Published under license by AIP Publishing.

thermal conductivity of hexagonal boron nitride with defects such as boron monovacancy, nitrogen monovacancy, and Stone-Wales defects. Fei *et al.*[15,16] have reported a $ZT \sim 1$ at room temperature (RT) for 2D-phosphorene. In the case of two-dimensional boron nitride, we have shown reduction in the lattice thermal conductivity by stacking.[17] We have also recently calculated the enhancement of ZT of graphene by doping it with dimers of boron nitride, which simultaneously increases the power factor ($S^2\sigma$)[18] and decreases the lattice thermal conductivity.[19]

There are various methods for doping in 2D materials. For example, n-type (p-type) doping can be achieved by donating (extracting) electrons from the 2D material.[20,21] n-type (p-type) doping can also be achieved by replacing the site atom with another atom having more (less) valence electrons than that of the site atoms.[22] These techniques have been done for MoS_2 and hence can be easily carried out on ZrX_2. Doping can also be achieved without randomly distributed impurities by electrolyte gating.[23,24]

Strain can be introduced in 2D materials by lattice mismatch between the substrates and epitaxial thin films.[25] By transferring a 2D material onto a substrate, strain can be induced on the 2D material by bending[26] or stretching[27] the substrate.

Several 2D materials under the influence of strain demonstrate a functional technique to tune the electronic band structure[5,15,28,29] and phonon dispersion.[29–31] Inducing strain on phosphorene has been shown to considerably enhance the Seebeck coefficient.[31] A solution to the phonon transport Boltzmann equation from molecular and lattice dynamics was carried out for graphene and boron nitride to study their nonmonotonic behavior of lattice thermal conductivity.[32] While the lattice thermal conductivity of graphene does not vary much with small strain,[32,33] there have been various reports on the investigation of the mode contributions to the lattice thermal conductivity.[33–36] Therefore, there is a need to investigate the mode dependence contribution to the lattice thermal conductivity, which, to the best of our knowledge, does not exist in the literature. In this paper, we therefore calculate the contribution to the lattice thermal conductivity of ZrX_2; X = S, Se, Te. Moreover, we calculate the figure of merit by calculating the electron relaxation time and electrical thermoelectric parameters, the electrical conductivity, and Seebeck coefficients.

Within the framework of density functional theory (DFT) and density functional perturbation theory (DFPT), we have recently reported results of the structural parameters, electronic band structure, and phonon dispersion for unstrained and strained (tensile and compressive) monolayers of ZrX_2 (X = S, Se, Te),[29] where the structure of the monolayers with lattice parameters is also given. Using these electronic and phonon band structure data, electrical and lattice transport parameters of ZrX_2 (X = S, Se, Te) monolayers are obtained using semiclassical electrical and phonon Boltzmann transport equations (BTEs), respectively. To calculate the electrical conductivity and Seebeck coefficients, the electrical BTE is applied to the band electrons derived from DFT, in the relaxation time approximation (RTA), as implemented in the BoltzTraP code.[37] Similarly, the lattice thermal conductivity (κ_L) is calculated by solving the phonon BTE, applied beyond the RTA, using a real-space supercell approach using the phonon dispersion derived from DFPT as implemented in the ShengBTE code.[38]

A. Electrical Boltzmann transport equations

The electrical BTE calculates the transport properties along the two orthogonal principal axes in the xy-plane. The S and σ values are averaged over these principal directions. The velocities of the electrons can be determined from the energies (ε) and wave-vector ($\mathbf{k}$) points derived from DFT. The expression for the wave-dependent velocity [$v_\alpha(i, \mathbf{k})$] in the ith band is given by

$$v_\alpha(i, \mathbf{k}) = \frac{1}{\hbar}\frac{\partial \varepsilon_{i,k}}{\partial k_\alpha}, \tag{1}$$

where α denotes the velocity's component. In the RTA, σ and S tensors are expressed in terms of the electron velocities as[37]

$$\sigma_{\alpha\beta}(T, \mu) = \frac{1}{V}\int \tau_e e^2 v_\alpha(i, \mathbf{k})\, v_\beta(i, \mathbf{k})\left[\frac{-\partial f_\mu(T, \epsilon)}{\partial \epsilon}\right] d\epsilon \tag{2}$$

and

$$S_{\alpha\beta} = \frac{1}{eT}\frac{\int \tau_e v_\alpha(i, \mathbf{k}) v_\beta(i, \mathbf{k})(\epsilon - \mu)\left[\frac{-\partial f_\mu(T, \epsilon)}{\partial \epsilon}\right] d\epsilon}{\int \tau_e v_\alpha(i, \mathbf{k}) v_\beta(i, \mathbf{k})\left[\frac{-\partial f_\mu(T, \epsilon)}{\partial \epsilon}\right] d\epsilon}. \tag{3}$$

Here, the electron relaxation time, Fermi-Dirac distribution, chemical potential, volume of the unit cell, absolute temperature, and Boltzmann constant are denoted by τ_e, $f_\mu = \frac{1}{1+e^{\frac{\epsilon-\mu}{k_B T}}}$, μ, V, T, and k_B, respectively.

B. Electrical relaxation time

In order to estimate the electrical relaxation time, we employ the model[39,40] as implemented in the BoltzTrap code, where

$$\tau(E, T) = \tau_0\left(\frac{E - E_{VBM/CBM}}{k_B T}\right)^{r-\frac{1}{2}}\left(\frac{T_0}{T}\right)^{l}. \tag{4}$$

Here, $E_{VBM(CBM)}$ is the valence band maximum (conduction band minimum) for the p-type (n-type) conduction. τ_0 is the reference lifetime, specified at some reference temperature T_0. The exponent of energy r, known as the scattering parameter, and the exponent of the temperature dependence, l, have the following values for different scattering mechanisms: (i) Scattering due to acoustic phonons in 2D (3D) materials, $r = \frac{3}{2}$ ($r = 2$) and $l = 0$, and (ii) $r = 1$ and $l = 1$ for scattering by optical phonons at high temperatures. Moreover, an l value of -3 (-4) would implement effects due to scattering based on phonon isotopes (normal phonon). The scattering parameter r cannot be negative. However, if the Fermi energy is so low that scattering angles up to π are allowed, $r = 0$. More detailed information about the method has been reported by Durczewski and Ausloos,[40] Okuda *et al.*,[41] and Palmer *et al.*[42]

C. Phonon Boltzmann transport equations

The calculations of the lattice thermal conductivity (κ_L) require the second-order (harmonic) and third-order (anharmonic)

Published under license by AIP Publishing.

interatomic force constants (IFCs). The harmonic IFCs have been calculated by us earlier to obtain the phonon dispersion.[29] We therefore have to calculate only the third-order IFCs and thereafter obtain the lattice thermal conductivity.

Expanding the potential energy (E) around its equilibrium energy (E_0), we obtain the nth order IFCs (ϕ), which are the coefficients of the nth order term,

$$E = E_0 + \frac{1}{2}\sum_{ij\alpha\beta} \phi_{ij}^{\alpha\beta} r_i^\alpha r_j^\beta + \frac{1}{3!}\sum_{ijk\alpha\beta\gamma} \phi_{ijk}^{\alpha\beta\gamma} r_i^\alpha r_j^\beta r_k^\gamma + \cdots. \quad (5)$$

The third-order IFCs can therefore be expressed as

$$\phi_{ijk}^{\alpha\beta\gamma} = \frac{\partial^3 E}{\partial r_i^\alpha \partial r_j^\beta \partial r_k^\gamma}. \quad (6)$$

Using the finite difference method, Eq. (6) can be approximately expressed as

$$\phi_{ijk}^{\alpha\beta\gamma} \approx \frac{1}{4h^2}[-F_k^\gamma(r_i^\alpha = h, r_j^\beta = h) + F_k^\gamma(r_i^\alpha = h, r_j^\beta = -h) + F_k^\gamma(r_i^\alpha = -h, r_j^\beta = h) - F_k^\gamma(r_i^\alpha = -h, r_j^\beta = -h)], \quad (7)$$

where h is an arbitrary small displacement from the system's equilibrium position. F_k^γ is the γ component of the force experienced by the kth atom. We use the "thirdorder.py" python script, which is part of the ShengBTE package to generate different configurations having displaced atoms. The number of configurations created depends on the number of nearest neighbor interactions, symmetry of the system, size of the supercell mesh, and size of the unit cell. In all of our calculations, the supercell mesh size was fixed at $3 \times 3 \times 3$. The number of nearest neighbor interactions was chosen to be four. 300 and 372 configurations were generated for each system with and without strain, respectively. Note that the difference in the number of configurations is due to the change in the symmetry of the system under the influence of strain.

After obtaining harmonic and anharmonic terms, the lattice thermal conductivity tensor is then calculated beyond the RTA using the following expression:

$$\kappa_L^{\alpha\beta} = \frac{1}{k_B T^2 VN}\sum_\lambda f_0(f_0+1)(\hbar\omega_\lambda)^2 v_\lambda^\alpha \tau_\lambda^0 (v_\lambda^\beta + \Delta_\lambda^\beta). \quad (8)$$

Here, N is the total number of sampling wave-vector ($\mathbf{q}$) points (we use a different notation here because the points correspond to that of phonons). The size of the grid plane mesh along each axis in the reciprocal space was chosen to be $24 \times 24 \times 1$ for all our calculations. τ^0 represents the relaxation time, λ corresponds to the acoustic and optical modes and v the phonon group velocity. The Bose-Einstein distribution is $f_0 = \frac{1}{e^{\frac{\hbar\omega}{k_B T}} - 1}$, where $\hbar$ and ω are Planck's constant and phonon frequency. It is evident from Eq. (8) that setting $\Delta = 0$ is identical to solving the phonon BTE in the RTA. Therefore, Δ is a measure how much the associated heat current of a particular phonon mode deviates from the RTA solution of the phonon BTE. Δ is a function of the three-phonon processes and the scattering probabilities from isotropic disorders. The three-phonon scattering amplitudes, which are a function of the third-order anharmonic term, are then computed from the derivatives of energy obtained from DFT using the QUANTUM ESPRESSO code.[43] Using the ShengBTE code, the relaxation times are obtained by an iterative method with the initial run as the RTA, i.e., $\Delta = 0$. Iterations stop when two successive runs for Δ (and hence τ) have a difference of 10^{-5} $\mathrm{Wm^{-1}\,K^{-1}}$.

In order to get an estimate of the lattice thermal conductivity as a function of its sample length, we calculate the cumulative κ_L since the mean-free path (MFP) cannot be larger in size than the physical sample length of the sheet. The cumulative κ_L is obtained by permitting only phonons with a MFP below some certain threshold value. The cumulative κ_L is then fitted to the form[38]

$$\kappa_L(L) = \frac{\kappa_{L_{\max}}}{1 + \frac{L_0}{L}}, \quad (9)$$

where $\kappa_{L_{\max}}$ is the thermodynamic limit of lattice thermal conductivity, i.e., κ_L as $L \to \infty$. L_0 is a fitting parameter and L is the MFP (or the sample length of the sheet). Detailed information and workflow have been reported by Li *et al.*[38]

II. RESULTS AND DISCUSSIONS

A. Electrical Boltzmann transport

Using the Boltzmann transport equation (BTE) for the band electrons, we calculate the scaled electrical conductivity ($\frac{\sigma}{\tau_e}$; τ_e is the electrical relaxation time), Seebeck coefficient, and power factor ($S^2\sigma$). The Seebeck coefficient, from its definition [Eq. (3)], can be shown to be independent of its electrical relaxation time.

In Fig. 1, we present the electronic transport parameters of ZrX_2 as a function of its charge carriers for unstrained (black curves), 6% biaxial strain (red curves), and 10% biaxial strain (blue curves). There is a general trend that all n-type doped systems have a larger power factor in comparison with their corresponding p-type doping. This behavior can be attributed to the larger effective mass in n-type doped systems in ZrX_2. Therefore, our calculations suggest that n-type doping would yield better results for an enhanced thermoelectric performance.

The most interesting feature is that the maximum of the power factor for ZrS_2 and $ZrSe_2$ is for a tensile strain of 6%, while that of $ZrTe_2$ is 10%. The reason for this can be understood with the analogy of doping boron nitride with graphene. Doping boron nitride with graphene modulates the electronic bandgap[44–46] just like applying strain in ZrX_2. We have shown recently[29] that the bandgap of ZrX_2 has a maximum at 6% for X = S, Se, while the bandgap keeps increasing with tensile strain for X = Te. Since ZrX_2 are either metals or semiconductors, it can be shown that a Sommerfeld expansion around the Fermi energy yields Mott's formula, $S \propto \frac{1}{\sigma}\frac{d\sigma}{d\mu}$. Therefore, from Mott's formula, it is seen that the two competing contributions to S are σ^{-1} and $\frac{d\sigma}{d\mu}$. If the shape of the band structure does not change much, the major

Published under license by AIP Publishing.

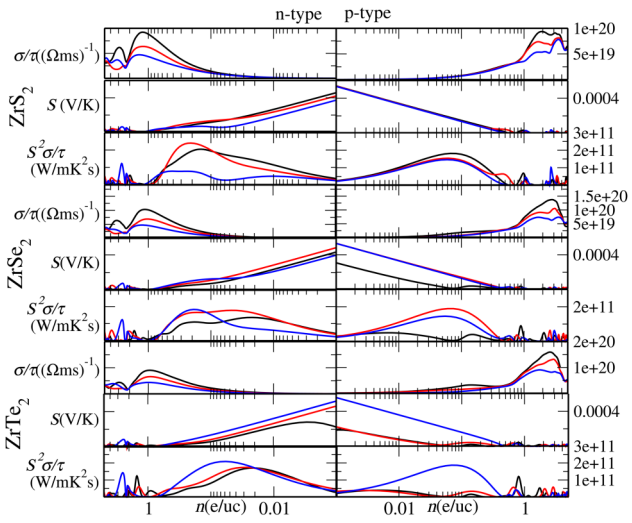


FIG. 1. Electronic transport parameters as a function of its charge carrier (number of electrons per unit cell) for ZrX_2; X = S, Se, Te. The first three rows are the scaled electrical conductivity, Seebeck coefficient, and power factor for ZrS_2, respectively. Similarly, the next three are for $ZrSe_2$ and the last three are for $ZrTe_2$. The black curves represent unstrained ZrX_2, while red and blue curves represent a biaxial strain of 6% and 10%, respectively. The two columns correspond to *n*-type (left) and *p*-type (right) doping.

contribution to S would be from σ^{-1}. The band structure calculations do show that the shape of the bands is not much affected. However, the bandgap increases with tensile strain. A large bandgap implies a lower electrical conductivity, thus producing a larger S. This explains the maximum power factor in ZrX_2 for each case. Similar results for ZrS_2[47] and $ZrSe_2$[48] have been reported and are in excellent agreement with our calculations. However, they do not offer an explanation for such behavior. We would like to stress the fact that, against the popular belief that lower electrical conductivity is detrimental to ZT, Mott's formula shows that lower conductivity for metals and semiconductors would actually increase the Seebeck coefficients, thus increasing the power factor, which is proportional to the square of S.

In Fig. 2, we plot the power factor as a function of its charge carrier concentration at temperatures $T = 300$ K, 450 K, 600 K, 750 K, and 900 K. A common trend in the behavior of the ZrX_2 power factor is that it increases with the temperature. Moreover, only near $|n| \sim 0$, higher the temperature, the peak of the power factor shifts to a higher value of $|n|$. This behavior can be ascribed to the more thermally excited electrons since $|n| \sim 0$ implies that the chemical potential is near the Fermi energy. Therefore, the concentration of electrons would increase due to the availability of energy states above the ground state. Higher temperature would also imply more thermally excited electrons.

We next consider the effect of tensile strains on the lattice thermal conductivity of ZrX_2 since Seebeck coefficients and the power factor increase due to strain, thus improving the thermoelectric figure of merit.

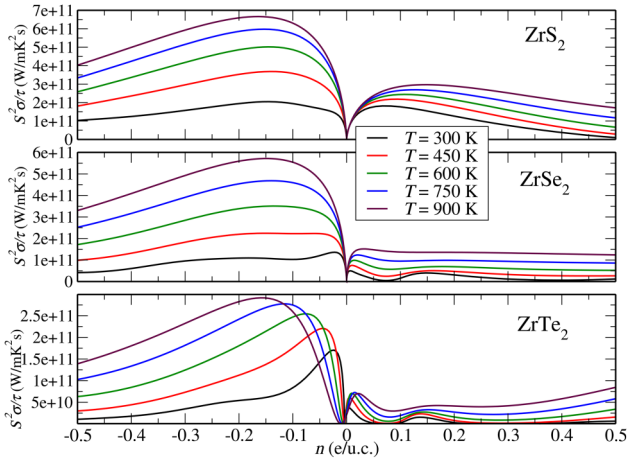


FIG. 2. Power factor of ZrX_2 as a function of the charge carrier at five different temperatures, $T = 300$ K, 450 K, 600 K, 750 K, and 900 K.

B. Effective mass and electron relaxation time

In Sec. II A, we presented the scaled electrical conductivity and Seebeck coefficients. However, in order to calculate the power factor, one would require the electrical relaxation time. Previously, we compared our scaled electrical conductivity with experiments to get an estimate for the electrical relaxation time, for example, with graphene[19] and graphene/boron nitride heterostructures.[49] In the case of ZrX_2, to the best of our knowledge, no experiments have been reported to compare our scaled electrical conductivity. Therefore, in this section, we calculate the relaxation time using Eq. (4).

One would require the reference lifetime, scattering parameter, and temperature dependence to have an accurate estimate of the electrical relaxation time. The reference lifetime can be estimated from the fact that the electron scattering rate is given by Fermi's golden rule,[50]

$$\tau_e = \frac{\hbar}{2\pi g(E)|\langle f|H'|i\rangle|^2}, \tag{10}$$

where $g(E)$ is the energy density of state and is proportional to the directional effective mass. $\langle f|H'|i\rangle$ is the matrix element of the perturbation Hamiltonian H' between the final ($\langle f|$) state and initial state ($|i\rangle$). Thermoelectric materials exhibit directional behavior mainly from the directional effective masses. The directional effective mass was calculated by approximating the electronic band structure around the valence band maximum and conduction band minimum to be parabolic,

$$E = \frac{\hbar^2}{2}\left(\frac{k_x^2}{m_x} + \frac{k_y^2}{m_y}\right). \tag{11}$$

Here, m_x and m_y are the principal directional effective masses. k_x and k_y are the components of the wavevector with a magnitude

Published under license by AIP Publishing.

expressed as $k = \sqrt{k_x^2 + k_y^2}$. We define a new wavevector, k', and an effective mass, m', for the system by the relation

$$E = \frac{\hbar^2 k'^2}{2m'} = \frac{\hbar^2 (k_x'^2 + k_y'^2)}{2m'}. \tag{12}$$

The relation between the new proposed wavevector and effective mass with the components of the wavevector and directional effective masses is thus given by

$$k_x(y) = \sqrt{\frac{m_{x(y)}}{m'}} k'_{x(y)}. \tag{13}$$

The infinitesimal surface area element for a two-dimensional material is expressed as

$$\begin{aligned} dk = dk_x dk_y &= \sqrt{\frac{m_x m_y}{m'^2}} dk'_x dk'_y \\ &= \sqrt{\frac{m_x m_y}{m'^2}} 2\pi k' dk'. \end{aligned} \tag{14}$$

The density of states is then calculated by counting the number of states between k and $k + dk$ in a two-dimensional space divided by the smallest area of the wavevector in a crystal, $\left(\frac{2\pi}{L}\right)^2$. Accounting for the electron spin, Pauli exclusion principle, the density of states, $g(k)dk$, is expressed as

$$g(k)dk = \left(\frac{\sqrt{m_x m_y}}{\pi}\right) \frac{k' dk'}{m'}. \tag{15}$$

By differentiating Eq. (12) and by substituting $\frac{k' dk'}{m'}$ in Eq. (15), the energy density of states is expressed as

$$g(E) = \left(\frac{\sqrt{m_x m_y}}{\pi}\right) \left(\frac{1}{\hbar^2}\right). \tag{16}$$

From Eq. (10), the scattering lifetime is given by

$$\tau_e = \left(\frac{\pi}{\sqrt{m_x m_y}}\right) \left(\frac{\hbar}{2\pi}\right) \left(\frac{\hbar^2}{|\langle f|H'|i\rangle|^2}\right). \tag{17}$$

The calculation of the matrix element in Eq. (17) is beyond the scope of this paper. However, it is a constant, and its value would be governed by the deformation potential.

The deformation potential has been shown to be ∼1 eV for ZrX_2 materials. For example, the deformation potentials for ZrS_2 and $ZrSe_2$ are 1.52 eV and 1.25 eV, respectively.[51]

We thus choose Eq. (17) as the reference lifetime in our calculations with $|\langle f|H'|i\rangle|^2 \sim 1$ eV.

In Fig. 3, we plot the band structure for the valence band maximum and conduction band minimum for unstrained and 6% strain ZrX_2. The black (red) curves refer to that of the unstrained (strained) systems. The circular points refer to that of the parabolic curve as shown in Eq. (12), with m' as the fitting parameter. The values of m' are shown in Table I. The parabolic fit represents the actual band structure well for values around the valence band maximum and conduction band minimum, implying that the effective mass at the valence band maximum and conduction band minimum is extremely accurate.

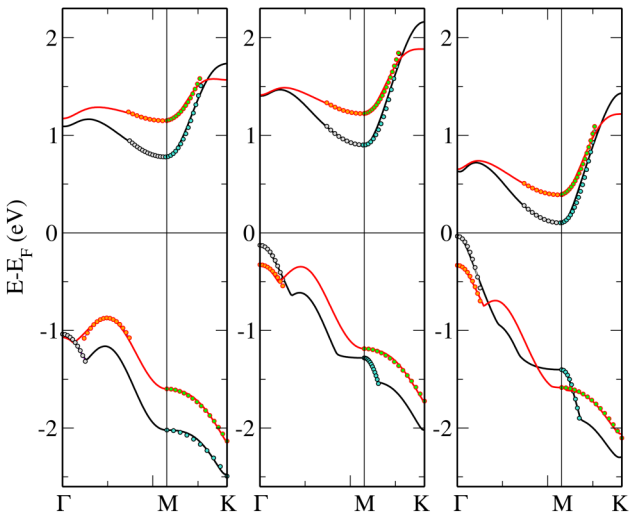


FIG. 3. The valence band maximum and conduction band minimum for unstrained and 6% strain ZrX_2. The circular points refer to that of the parabolic curve [Eq. (12)].

The scattering parameters were chosen to be $r = \frac{3}{2}$ and $p = 0$ since these values are a typical trait of deformation potential scattering by alloys of 2D materials as mentioned in Sec. I B.

In Fig. 4, we plot the relaxation time of ZrX_2 as a function of n-type and p-type charge carriers. There have been earlier reports estimating the relaxation time for ZrX_2 (X = S, Se),[47,48] which are of the same order of magnitude with our calculations. However, those methods use a constant τ_e for a given temperature. Our calculated τ_e, being a function of charge carrier (and hence chemical potential), would demonstrate characteristics observed experimentally.

TABLE I. Effective masses of unstrained ZrX_2 and under 6% tensile strain at the valence band maximum and conduction band minimum for two perpendicular directions along the high symmetric points, ΓM and KM.

		0% strain		6% strain	
		e	h	e	h
ZrS_2	$m_{\Gamma M}$	2.543	0.608	4.175	0.720
	m_{MK}	0.556	2.503	0.841	1.966
$ZrSe_2$	$m_{\Gamma M}$	2.247	0.455	3.250	0.658
	m_{MK}	0.399	0.236	0.556	1.857
$ZrTe_2$	$m_{\Gamma M}$	2.075	0.273	2.591	0.351
	m_{MK}	0.350	0.176	0.443	1.742

Published under license by AIP Publishing.

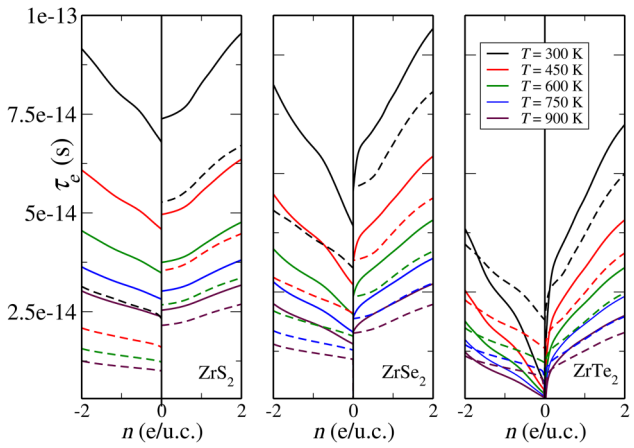


FIG. 4. The electron relaxation time as a function of *n*-type and *p*-type charge carriers for unstrained and 6% tensile strain ZrX_2. The straight (dotted) curves refer to that of the unstrained (6% tensile strain) ZrX_2.

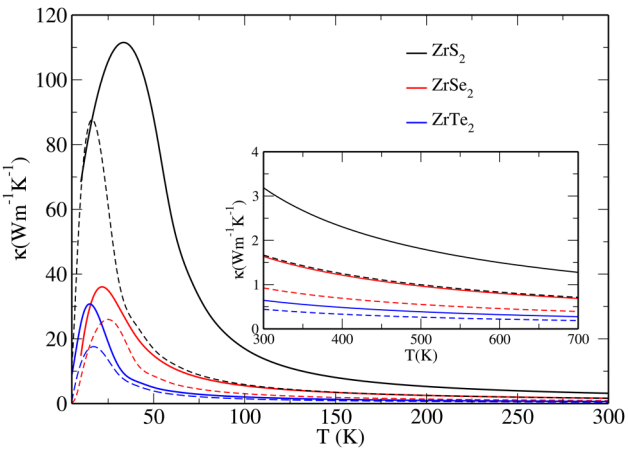


FIG. 5. Lattice thermal conductivity of unstrained (solid lines) and 6% tensile strain (dashed lines) ZrX_2 as a function of temperature.

For example, the relaxation time for 2D graphene has been reported by Tan *et al.*[52] It can be seen that while the magnitude of the charge carriers increase, τ_e increases, in-line with our calculations. For semiconductors, the width of the bandgap is small enough for an electron from the valence band to enter the conduction band. Therefore, a larger concentration of electrons and holes would imply larger electrical conductivity and hence higher relaxation times. It can also be seen that for higher temperature, the relaxation time decreases. This is due to the increased thermal velocity, which increases the collision between electrons, thus reducing τ_e. Under the impact of tensile strain, the relaxation time decreases for ZrX_2. This characteristic can be understood due to the increased effective mass as seen from Table I.

C. Lattice thermal Boltzmann transport

The phonon dispersion plays a vital role in investigating the lattice thermal conductivity. Very recently, we calculated the phonon dispersion of unstrained and 6% biaxial tensile ZrX_2 and found no imaginary frequencies in either of the systems, thus confirming its thermal stability.[29] The temperature dependence of the lattice thermal conductivity (κ_L) of unstrained and 6% tensile strain ZrX_2 is shown in Fig. 5. For clarity, in the inset of Fig. 5, we plot κ_L in the $T = 300$–700 K temperature range. It is observed that the variation of κ_L is the maximum in the case of ZrS_2, followed by $ZrSe_2$ and $ZrTe_2$. This behavior can be explained as follows. The acoustic modes contribute almost entirely to κ_L. As we move from S to Se to Te, the maximum acoustic frequencies keep reducing. This results in lower group velocities. Therefore, from Eq. (8), having reduced ω and v would result in lower κ_L. By the definition of the dynamical matrix, it can be seen that the phonon frequencies are proportional to the reciprocal of the atomic masses in the unit cell. It therefore follows that within a particular group, κ_L would reduce if the constituent atoms are positioned comparatively lower in the periodic table. For example, $MoSe_2$[53] has a lower κ_L in comparison with MoS_2.[54] Similarly, very recently, Mobaraki *et al.*[55] showed that WSe_2 demonstrates a lower κ_L relative to WS_2. Moreover, $ZrTe_2$ would have an even smaller κ_L due to the fact that the optical modes and acoustic modes are coupled[29] unlike in the case of ZrS_2, MoS_2, and WS_2. Even the optical modes and acoustic modes are separated by a tiny frequency gap in $ZrSe_2$. In the small frequency range where the optical modes couple with the acoustic mode, the scattering rates in phonons would therefore increase, thus resulting in an even lower κ_L.

Figure 6 shows the temperature dependence of the total thermal conductivity for different sample lengths, $L = 5$ nm, 25 nm, 50 nm, and 100 nm. In all cases, it is observed that, for the smallest length, $L = 5$ nm, κ_L initially increases but then at higher

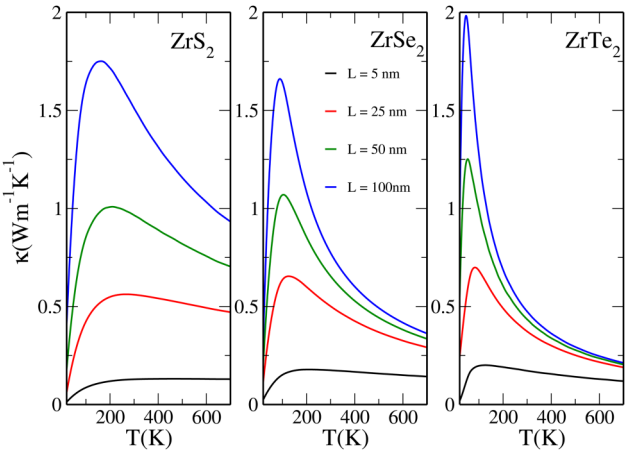


FIG. 6. Lattice thermal conductivity of ZrX_2 at constant lengths, 5 nm, 25 nm, 50 nm, and 100 nm.

Published under license by AIP Publishing.

temperatures, $T > 100$ K, has a slight or no dependency with temperature (T). The T dependencies increase as the sample length of the system increases. Around $L = 100$ nm, the $\frac{1}{T}$ dependence starts to form. This characteristic can be understood by recalling the scattering rates that contribute to the total phonon relaxation time. The boundary scattering $\frac{1}{\tau_B}$ is inversely proportional to length and has no temperature dependence, while the anharmonic scattering rates have a $\frac{1}{T}$ dependence. Therefore, by Matthiessen's rule,[56] the total phonon relaxation time is almost entirely dominated by the τ_B for extremely small sample lengths. With increase in the sample length, the contribution from the boundary scattering therefore decreases. The dominant scattering is now the anharmonic scattering rates, and hence, the $\frac{1}{T}$ dependencies of temperature start to form.

In all of our calculations, the biaxial strain reduces the lattice thermal conductivity. To have a better understanding of the influence of strain in κ_L, we inspect the mode dependence of $ZrTe_2$. In Fig. 7(a), we plot the phonon lifetimes contributed from boundary scattering (per mean-free path), isotopic scattering, and anharmonic scattering of each acoustic mode for unstrained and 6% tensile strain $ZrTe_2$. The phonon lifetimes are comparatively larger for smaller wavelengths, indicating that heat is being transferred predominantly by acoustic phonons. Additionally, at smaller wavelengths, the phonon dispersions do not couple with each other, and, therefore, the phonon-phonon scattering rates are low. Our calculations clearly show that the dominant scattering is due to the anharmonic scattering rates. Moreover, except for the anharmonic scattering rates from the ZA modes, the mode dependence calculation of phonon lifetimes shows very little dependency with strain, implying that tensile strain decreases the phonon lifetime of the ZA mode. The decrement of the anharmonic scattering occurring at lower frequencies can be inferred as follows. Tensile strain on the ZA mode of $ZrTe_2$ transforms the quadratic behavior at lower frequencies to a more linear phonon dispersion, thus decreasing the phonon density of states[19] and therefore decreasing the phonon lifetimes of the ZA mode. Our calculation of scattering rates could be verified using experimental techniques such as inelastic neutron or X-ray scattering.[57]

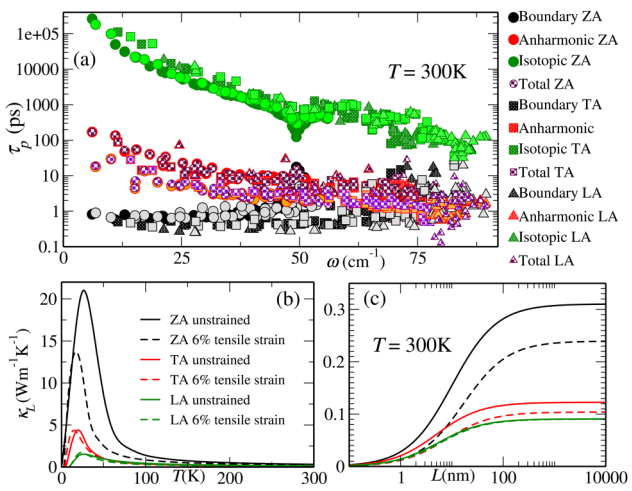


FIG. 7. (a) The phonon lifetime contributions, i.e., boundary scattering (per unit length), anharmonic scattering, and isotopic scattering, from each of the acoustic modes to the total thermal conductivity for $ZrTe_2$. Legends for the unstrained case are shown to the right of (a), whereas legends with the similar symbols but of different colors refer to the scattering rates for $ZrTe_2$ with 6% strain. (b) and (c) Acoustic mode contribution to the total lattice thermal conductivity (b) as a function of temperature and (c) as a function of sample length at room temperature. The out-of-plane acoustic modes are denoted by black curves, while the in-plane acoustic modes are denoted by red for the transverse acoustic (TA) modes and green for the longitudinal acoustic (LA) modes. Solid curves refer to the unstrained system, while the dotted curves correspond to the 6% strain strained system.

In Fig. 7(b), we plot the acoustic mode contributions to κ_L. The optical modes contribute negligibly to κ_L since the phonon scattering rates are large and the group velocities are small in comparison with the acoustic modes. The out-of-plane acoustic flexural modes (ZA) are shown in black. The transverse (TA) and longitudinal acoustic (LA) modes are shown in red and green, respectively. The solid and dotted lines refer to that of unstrained and 6% biaxial tensile strain.

Our calculations demonstrate that the ZA modes contribute maximally to κ_L with little effects from TA and LA modes. The majority of ZA modes contributing to κ_L is in-line with the mode contributions seen in MoS_2.[54] The rotational symmetry of the out-of-plane mode, which causes the quadratic nature of the ZA modes near the high symmetric Γ point, corresponds to the large density of flexural phonons. An applied strain softens the in-plane (TA and LA) modes, while it stiffens the out-of-plane modes. A biaxial tensile strain gradually changes the quadratic nature of the ZA mode to a linear nature, thus implying a break in the rotational symmetry and resulting in a decrease in the contribution from the ZA mode. For a sufficiently large strain, the ZA modes becomes linear and will contribute less in comparison with the LA and TA mode. Such a trend has been seen in $2H - MoTe_2$.[58] A tensile strain would always decrease the thermal conductivity if the system does not have reflection symmetry.[58]

In Fig. 7(c), we plot the mode contribution to κ_L as a function of length. The maximum increase in κ_L is seen at lower lengths. As mentioned earlier, since τ_B dominates for small mean-free paths, κ_L increases linearly at smaller sample lengths. For larger lengths, the anharmonic scattering rates, which have no length dependence, dominate. This therefore results in a constant κ_L. It is precisely because of the behavior of κ_L as a function of L that nanostructuring and doping result in decreasing κ_L. Nanostructuring and doping further decrease the phonon mean-free path and therefore must be operated at lengths where the boundary scattering dominates the total scattering rates. It can also be seen from Figs. 7(b) and 7(c) that summing the contribution from LA and TA would contribute almost the same amount to κ_L as that of those from ZA modes. A strain larger than 6% would therefore imply that the dominant contribution to κ_L at room temperature would be from in-plane modes and not from out-of-plane modes.

D. Figure of merit

Having calculated all the thermoelectric parameters required for the conversion efficiency of ZrX_2, we can now compute the

Published under license by AIP Publishing.

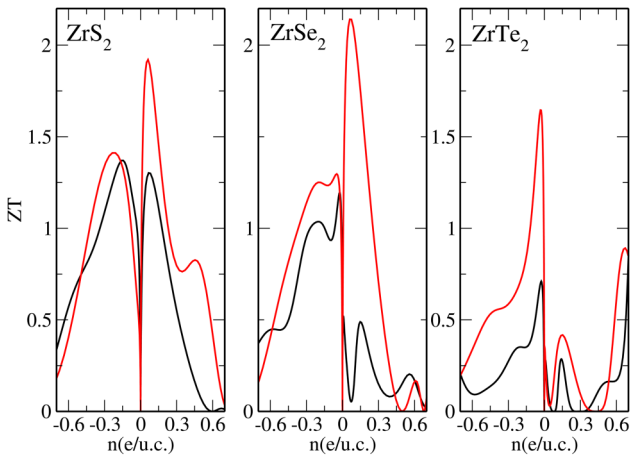


FIG. 8. The figure of merit of unstrained and 6% tensile ZrX_2. The black curves refer to that of the unstrained systems, while the red curves refer to that of the tensile strain.

figure of merit, $ZT = \frac{\tau_e(\frac{\sigma}{\tau_e})S^2T}{\kappa}$. In Fig. 8, we plot the room temperature figure of merit of unstrained and 6% tensile strain ZrX_2 at the thermodynamic limit. Our calculations clearly show that ZT of group IV TMDs are good candidates for 2D thermoelectric materials. As expected, we find a large enhancement in ZT when the system is under a biaxial tensile strain. The enhancement of ZT is due to the simultaneous increase in the power factor and decrease in the lattice thermal conductivity. An interesting observation in our calculations reveal that, for ZrS_2 and $ZrSe_2$, under tensile strain, the p-type doping results in a superior thermoelectric performance, while the reverse is observed for n-type doping. This is in-line with another ZrS_2 report.[47] For the case in $ZrTe_2$, n-type doping would result in an enhanced ZT with and without an impact in tensile strain. The extent in the enhancement of ZT in ZrS_2 in our calculation is smaller than that seen in a recent previous report[47] since the effective mass calculated by us is larger, thus reducing the relaxation times and hence the power factor.

III. CONCLUSION

To summarize, using first-principles methods, we have calculated all the thermoelectric parameters required to obtain the figure of merit of ZrX_2. Parameters related to electrons, such as electrical conductivities, Seebeck coefficients, and electron relaxation times were calculated using the electron Boltzmann equations on band electrons derived from density functional theory. The parameter related to phonons, i.e., the lattice thermal conductivity, was calculated using the phonon BTE from the phonon dispersion and interatomic force constant extracted from density functional perturbation theory. Our calculations demonstrate that tensile strain in ZrX_2 would enhance the figure of merit by simultaneously increasing the power factor and reducing the lattice thermal conductivity.

Power-factor calculations of unstrained ZrX_2 suggest that n-type doped systems yield better thermoelectric performance than their p-type counterpart. Moreover, higher temperature yields a higher power factor, with the maximum corresponding to larger charge carriers due to excited electrons. Under the influence of tensile strain, the maximum power factor as a function of charge carriers (or chemical potential) is found to be when the system has the maximum bandgap. We interpret these results using Mott's formula, which shows that the Seebeck coefficient is proportional to the inverse of electrical conductivity and the derivative of the electrical conductivity. Since the shape of the bands does not change much, the Seebeck coefficient is highly dependent on the inverse electrical conductivity. Therefore, larger bandgap would imply lower conductivity and, hence, higher Seebeck coefficients and a higher power factor.

Room temperature lattice thermal conductivity calculations show that the largest κ_L is for ZrS_2 and then $ZrSe_2$ and the lowest for $ZrTe_2$ since the highest acoustic frequencies and velocities keep reducing as we move from ZrS_2 to $ZrSe_2$ to $ZrTe_2$. Length dependent calculations show that there is little or no temperature dependence for κ_L at small sample lengths ($L = 5$ nm), while it displays a T^{-1} temperature dependence at larger sample lengths ($L = 100$ nm). This is due to the boundary scattering rates, which dominate at small sample lengths, while the anharmonic scattering rates dominate at larger sample lengths.

Mode dependent calculations were carried out to understand the reduction in the lattice thermal conductivity due to tensile strain. The in-plane longitudinal and transverse acoustic modes were not affected to a large extent due to tensile strain, while the out-of-plane modes were greatly reduced. The calculations on phonon lifetimes also demonstrate that anharmonic scattering rates of ZA modes were affected the most due to tensile strain, thus lowering the out-of-plane ZA phonon lifetime. Our mode dependent calculations also suggest that for strains larger than 6%, the dominant modes contributing to the lattice thermal conductivity would be due to the in-plane acoustic modes due to stiffening of the ZA modes.

The electrical relaxation time was calculated from the effective mass. The larger the magnitude of the charge carrier masses is, the larger the relaxation time, consistent with experimental observations. As for the dependence with temperature, the electrical relaxation time reduces with temperature because of its thermal velocity.

Finally, merging all the thermoelectric parameters together, we obtained the figure of merit of unstrained and 6% tensile strain ZrX_2. For (un)strained ZrS_2 and $ZrSe_2$, (n)p-type doping would yield superior ZT, while for $ZrTe_2$, n-type doping would yield better conversion efficiency. Our extensive study should provide useful information on the calculation of the thermoelectric figure of merit from atomic positions alone since our calculations are free of any fitting parameters. Since strain can be induced experimentally in 2D materials[25–27] and mode contribution to the lattice thermal conductivity can be measured,[59–61] our calculations should motivate similar experimental studies in 2D ZrX_2 monolayers.

ACKNOWLEDGMENTS

The calculations were performed in the High Performance Cluster platform at the S.N. Bose National Centre (SNBNCBS), which is funded by the Department of Science and Technology.

Published under license by AIP Publishing.

We are thankful to Peter Kratzer and Jesus Carrete for helpful correspondence. S.A. would like to express gratitude to King Khalid University, Abha, Saudi Arabia for providing administrative and technical support and acknowledges support of the Visitors Programme (EVLP) during a visit to SNBNCBS.

REFERENCES

[1]J. He, M. G. Kanatzidis, and V. P. Dravid, "High performance bulk thermoelectrics via a panoscopic approach," Mater. Today **16**, 166 (2013).
[2]J. Zhang, H. J. Liu, L. Cheng, J. Wei, J. H. Liang, D. D. Fan, J. Shi, X. F. Tang, and Q. J. Zhang, "Phosphorene nanoribbon as a promising candidate for thermoelectric applications," Sci. Rep. **4**, 6452 (2014).
[3]K. H. Park, P. N. Martin, and U. Ravaioli, "Electronic and thermal transport study of sinusoidally corrugated nanowires aiming to improve thermoelectric efficiency," Nanotechnology **27**, 035401 (2016).
[4]M. Buscema, M. Barkelid, V. Zwiller, H. S. J. van der Zant, G. A. Steele, and A. Castellanos-Gomez, "Large and tunable photothermoelectric effect in single-layer MoS_2," Nano Lett. **13**, 358 (2013).
[5]W. Huang, H. Da, and G. Liang, "Thermoelectric performance of MX_2 (M = Mo, W; X = S, Se) monolayers," J. Appl. Phys. **113**, 104304 (2013).
[6]D. Wickramaratne, F. Zahid, and R. K. Lake, "Electronic and thermoelectric properties of few-layer transition metal dichalcogenides," J. Chem. Phys. **140**, 124710 (2014).
[7]H. Babaei, J. M. Khodadadi, and S. Sinha, "Large theoretical thermoelectric power factor of suspended single-layer MoS_2," Appl. Phys. Lett. **105**, 193901 (2014).
[8]J. N. Coleman, M. Lotya, A. O'Neill, S. D. Bergin, P. J. King, U. Khan, K. Young, A. Gaucher, S. De, R. J. Smith, I. V. Shvets, S. K. Arora, G. Stanton, H.-Y. Kim, K. Lee, G. T. Kim, G. S. Duesberg, T. Hallam, J. J. Boland, J. J. Wang, J. F. Donegan, J. C. Grunlan, G. Moriarty, A. Shmeliov, R. J. Nicholls, J. M. Perkins, E. M. Grieveson, K. Theuwissen, D. W. McComb, P. D. Nellist, and V. Nicolosi, "Two-dimensional nanosheets produced by liquid exfoliation of layered materials," Science **331**, 568 (2011).
[9]S. Jeong, D. Yoo, M. Ahn, and P. Miró, "Tandem intercalation strategy for single-layer nanosheets as an effective alternative to conventional exfoliation processes," Nat. Commun. **6**, 5763 (2015).
[10]Z. Zeng, Z. Yin, X. Huang, H. Li, Q. He, G. Lu, F. Boey, and H. Zhang, "Single-layer semiconducting nanosheets: High-yield preparation and device fabrication," Angew. Chem. **50**, 11093 (2011).
[11]A. M. Sargar, N. S. Patil, S. R. Mane, S. N. Gawale, and P. N. Bhosale, "Electrochemical synthesis and characterisation of $ZrSe_2$ thin films," Int. J. Electrochem. Sci. **4**, 887 (2009); see http://www.electrochemsci.org/papers/vol4/4060887.pdf.
[12]P. Tsipas, D. Tsoutsou, S. Fragkos, R. Sant, C. Alvarez, H. Okuno, G. Renaud, R. Alcotte, T. Baron, and A. Dimoulas, "Massless dirac fermions in $ZrTe_2$ semimetal grown on InAs(111) by van der Waals epitaxy," ACS Nano **12**, 1696 (2018).
[13]Y. Anno, Y. Imakita, K. Takei, S. Akita, and T. Arie, "Enhancement of graphene thermoelectric performance through defect engineering," 2D Mater. **4**, 025019 (2017).
[14]A. Tabarraei, "Thermal conductivity of monolayer hexagonal boron nitride nanoribbons," Comput. Mater. Sci. **108**, 66 (2015).
[15]R. Fei, A. Faghaninia, R. Soklaski, J.-A. Yan, C. Lo, and L. Yang, "Enhanced thermoelectric efficiency via orthogonal electrical and thermal conductances in phosphorene," Nano Lett. **14**, 6393 (2014).
[16]R. Fei and L. Yang, "Strain-engineering the anisotropic electrical conductance of few-layer black phosphorus," Nano Lett. **14**, 2884 (2014).
[17]R. D'Souza and S. Mukherjee, "Length-dependent lattice thermal conductivity of single-layer and multilayer hexagonal boron nitride: A first-principles study using the Callaway-Klemens and real-space supercell methods," Phys. Rev. B **96**, 205422 (2017).
[18]R. D'Souza and S. Mukherjee, "First-principles study of the electrical and lattice thermal transport in monolayer and bilayer graphene," Phys. Rev. B **95**, 085435 (2017).
[19]R. D'Souza and S. Mukherjee, "Enhancement of thermoelectric figure-of-merit of graphene upon BN-doping and sample length reduction," J. Appl. Phys. **124**, 124301 (2018).
[20]S. Mouri, Y. Miyauchi, and K. Matsuda, "Tunable photoluminescence of monolayer MoS_2 via chemical doping," Nano Lett. **13**, 5944 (2013).
[21]D. Kiriya, M. Tosun, P. Zhao, J. S. Kang, and A. Javey, "Air-stable surface charge transfer doping of MoS_2 by benzyl viologen," J. Am. Chem. Soc. **136**, 7853 (2014).
[22]M. R. Laskar, D. N. Nath, L. Ma, E. W. Lee II, C. H. Lee, T. Kent, Z. Yang, R. Mishra, M. A. Roldan, J.-C. Idrobo, S. T. Pantelides, S. J. Pennycook, R. C. Myers, Y. Wu, and S. Rajan, "*p*-type doping of MoS_2 thin films using Nb," Appl. Phys. Lett. **104**, 092104 (2014).
[23]A. Das, S. Pisana, B. Chakraborty, S. Piscanec, S. K. Saha, U. V. Waghmare, K. S. Novoselov, H. R. Krishnamurthy, A. K. Geim, A. C. Ferrari, and A. K. Sood, "Monitoring dopants by Raman scattering in an electrochemically top-gated graphene transistor," Nat. Nanotechnol. **3**, 210 (2008).
[24]J. T. Ye, Y. J. Zhang, R. Akashi, M. S. Bahramy, R. Arita, and Y. Iwasa, "Superconducting dome in a gate-tuned band insulator," Science **338**, 1193 (2012).
[25]G. Gao, S. Jin, and W. Wu, "Lattice-mismatch-strain induced inhomogeneities in epitaxial $La_{0.7}Ca_{0.3}MnO_3$ films," Appl. Phys. Lett. **90**, 012509 (2007).
[26]S.-I. Park, J.-H. Ahn, X. Feng, S. Wang, Y. Huang, and J. A. Rogers, "Theoretical and experimental studies of bending of inorganic electronic materials on plastic substrates," Adv. Funct. Mater. **18**, 2673 (2008).
[27]K. S. Kim, Y. Zhao, H. Jang, S. Y. Lee, J. M. Kim, K. S. Kim, J.-H. Ahn, P. Kim, J.-Y. Choi, and B. H. Hong, "Large-scale pattern growth of graphene films for stretchable transparent electrodes," Nature **457**, 706 (2009).
[28]K. Ghosh and U. Singisetti, "Thermoelectric transport coefficients in monolayer MoS_2 and WSe_2: Role of substrate, interface phonons, plasmon, and dynamic screening," J. Appl. Phys. **118**, 135711 (2015).
[29]S. Ahmad, R. D'Souza, and S. Mukherjee, "Band gap modulation of ZrX_2 (X = S, Se, Te) mono-layers under biaxial strain and transverse electric field and its lattice dynamic properties: A first principles study," Mater. Res. Express **6**, 036308 (2019).
[30]M. Hu, X. Zhang, and D. Poulikakos, "Anomalous thermal response of silicene to uniaxial stretching," Phys. Rev. B **87**, 195417 (2013).
[31]L. Zhu, T. Zhang, Z. Sun, J. Li, G. Chen, and S. A. Yang, "Thermal conductivity of biaxial-strained MoS_2: Sensitive strain dependence and size-dependent reduction rate," Nanotechnology **26**, 465707 (2015).
[32]T. Zhu and E. Ertekin, "Resolving anomalous strain effects on two-dimensional phonon flows: The cases of graphene, boron nitride, and planar superlattices," Phys. Rev. B **91**, 205429 (2015).
[33]L. Lindsay, W. Li, J. Carrete, N. Mingo, D. A. Broido, and T. L. Reinecke, "Phonon thermal transport in strained and unstrained graphene from first principles," Phys. Rev. B **89**, 155426 (2014).
[34]Y. Kuang, L. Lindsay, S. Shi, X. Wang, and B. Huang, "Thermal conductivity of graphene mediated by strain and size," Int. J. Heat Mass Transf. **101**, 772 (2016).
[35]L. Lindsay, D. A. Broido, and N. Mingo, "Flexural phonons and thermal transport in multilayer graphene and graphite," Phys. Rev. B **83**, 235428 (2011).
[36]L. Lindsay, D. A. Broido, and N. Mingo, "Flexural phonons and thermal transport in graphene," Phys. Rev. B **82**, 115427 (2010).
[37]G. K. H. Madsen and D. J. Singh, "Boltztrap. A code for calculating band-structure dependent quantities," Comput. Phys. Commun. **175**, 67 (2006).
[38]W. Li, J. Carrete, N. A. Katcho, and N. Mingo, "ShengBTE: A solver of the Boltzmann transport equation for phonons," Comput. Phys. Commun. **185**, 1747 (2014).
[39]M. Zahedifar and P. Kratzer, "Band structure and thermoelectric properties of half-Heusler semiconductors from many-body perturbation theory," Phys. Rev. B **97**, 035204 (2018).

Published under license by AIP Publishing.

[40]K. Durczewski and M. Ausloos, "Nontrivial behavior of the thermoelectric power: Electron-electron versus electron-phonon scattering," Phys. Rev. B **97**, 5303 (2000).
[41]T. Okuda, K. Nakanishi, S. Miyasaka, and Y. Tokura, Phys. Rev. B **63**, 113104 (2001).
[42]M. A. Palmer, K. Bartkowski, E. Gmelin, M. Cardona, A. P. Zhernov, A. V. Inyushkin, A. Taldenkov, V. I. Ozhogin, K. M. Itoh, and E. E. Haller, "Thermal conductivity of germanium crystals with different isotopic compositions," Phys. Rev. B **56**, 9431 (1997).
[43]P. Giannozzi, S. Baroni, N. Bonini, M. Calandra, R. Car, C. Cavazzoni, D. Ceresoli, G. L. Chiarotti, M. Cococcioni, I. Dabo, A. D. Corso, S. de Gironcoli, S. Fabris, G. Fratesi, R. Gebauer, U. Gerstmann, C. Gougoussis, A. Kokalj, M. Lazzeri, L. Martin-Samos, N. Marzari, F. Mauri, R. Mazzarello, S. Paolini, A. Pasquarello, L. Paulatto, C. Sbraccia, S. Scandolo, G. Sclauzero, A. P. Seitsonen, A. Smogunov, P. Umari, and R. M. Wentzcovitch, "Quantum espresso: A modular and open-source software project for quantum simulations of materials," J. Phys. Condens. Matter **21**, 395502 (2009).
[44]R. D'Souza and S. Mukherjee, "Electronic structure, phase stability and resistivity of hybrid hexagonal $C_x(BN)_{1-x}$ two-dimensional nanomaterial: A first-principles study," Physica E **69**, 138 (2015).
[45]R. D'Souza, S. Mukherjee, and T. Saha-Dasgupta, "Influence of interface geometry on phase stability and bandgap engineering in boron nitride substituted graphene: A combined first-principles and Monte Carlo study," J. Alloys Compd. **708**, 437 (2017).
[46]M. Bernardi, M. Palummo, and J. Grossman, "Optoelectronic properties in monolayers of hybridized graphene and hexagonal boron nitride," Phys. Rev. Lett. **108**, 226805 (2012).
[47]H. Y. Lv, W. J. Lu, D. F. Shao, H. Y. Lu, and Y. P. Sun, "Strain-induced enhancement in the thermoelectric performance of a ZrS_2 monolayer," J. Mater. Chem. C **4**, 4538 (2016).
[48]G. Ding, G. Y. Gao, Z. Huang, W. Zhang, and K. Yao, "Thermoelectric properties of monolayer MSe_2 (M = Zr, Hf): Low lattice thermal conductivity and a promising figure of merit," Nanotechnology **27**, 375703 (2016).
[49]R. D'Souza and S. Mukherjee, "Thermoelectric transport in graphene/*h*-BN/graphene heterostructures: A computational study," Physica E **81**, 96 (2016).
[50]J. J. Sakurai, *Modern Quantum Mechanics* (Addison-Wesley, Reading, 1994).
[51]Z. Huang, W. Zhang, and W. Zhang, "Computational search for two-dimensional MX_2 semiconductors with possible high electron mobility at room temperature," Materials **9**, 716 (2016).
[52]Y. W. Tan, Y. Zhang, K. Bolotin, Y. Zhao, S. Adam, E. H. Hwang, S. D. Sarma, H. L. Stormer, and P. Kim, "Measurement of scattering rate and minimum conductivity in graphene," Phys. Rev. Lett. **99**, 246803 (2007).
[53]S. Kumar and U. Schwingenschlögl, "Thermoelectric response of bulk and monolayer $MoSe_2$ and WSe_2," Chem. Mater. **27**, 1278 (2015).
[54]W. Li, J. Carrete, and N. Mingo, "Thermal conductivity and phonon linewidths of monolayer MoS_2 from first principles," Appl. Phys. Lett. **103**, 253103 (2013).
[55]A. Mobaraki, A. Kandemir, H. Yapicioglu, O. Gölseren, and C. Sevik, "Validation of inter-atomic potential for WS_2 and WSe_2 crystals through assessment of thermal transport properties," Comput. Mater. Sci. **144**, 92 (2018).
[56]N. W. Ashcroft and N. D. Mermin, *Solid State Physics* (Holt, Rinehart and Winston, New York, 1976).
[57]J. W. L. Pang, W. J. L. Buyers, A. Chernatynskiy, M. D. Lumsden, B. C. Larson, and S. R. Phillpot, "Phonon lifetime investigation of anharmonicity and thermal conductivity of UO_2 by neutron scattering and theory," Phys. Rev. Lett. **110**, 157401 (2013).
[58]A. Shafique and Y.-H. Shin, "Strain engineering of phonon thermal transport properties in monolayer $2H - MoTe_2$," Phys. Chem. Chem. Phys. **19**, 32072 (2017).
[59]A. J. Minnich, J. A. Johnson, A. J. Schmidt, K. Esfarjani, M. S. Dresselhaus, K. A. Nelson, and G. Chen, "Thermal conductivity spectroscopy technique to measure phonon mean free paths," Phys. Rev. Lett. **107**, 095901 (2011).
[60]K. T. Regner, D. P. Sellan, Z. Su, C. H. Amon, A. J. H. McGaughey, and J. A. Malen, "Broadband phonon mean free path contributions to thermal conductivity measured using frequency domain thermoreflectance," Nat. Commun. **4**, 1640 (2013).
[61]J. A. Johnson, A. A. Maznev, J. Cuffe, J. K. Eliason, A. J. Minnich, T. Kehoe, C. M. S. Torres, G. Chen, and K. A. Nelson, "Direct measurement of room-temperature nondiffusive thermal transport over micron distances in a silicon membrane," Phys. Rev. Lett. **110**, 025901 (2013).

Published under license by AIP Publishing.